Estimating Profiles of Dissipation Rate in the Upper Ocean Using Acoustic Doppler Measurements Made from Surface-Following Platforms

KRISTIN ZEIDEN,[a] JIM THOMSON,[a] AND JAMES GIRTON[a]

[a] *Applied Physics Laboratory, University of Washington, Seattle, Washington*

ABSTRACT: High-resolution profiles of vertical velocity obtained from two different surface-following autonomous platforms, Surface Wave Instrument Floats with Tracking (SWIFTs) and a Liquid Robotics SV3 Wave Glider, are used to compute dissipation rate profiles $\epsilon(z)$ between 0.5 and 5 m depth via the structure function method. The main contribution of this work is to update previous SWIFT methods to account for bias due to surface gravity waves, which are ubiquitous in the near-surface region. We present a technique where the data are prefiltered by removing profiles of wave orbital velocities obtained via empirical orthogonal function (EOF) analysis of the data prior to computing the structure function. Our analysis builds on previous work to remove wave bias in which analytic modifications are made to the structure function model. However, we find the analytic approach less able to resolve the strong vertical gradients in $\epsilon(z)$ near the surface. The strength of the EOF filtering technique is that it does not require any assumptions about the structure of nonturbulent shear, and does not add any additional degrees of freedom in the least squares fit to the model of the structure function. In comparison to the analytic method, $\epsilon(z)$ estimates obtained via empirical filtering have substantially reduced noise and a clearer dependence on near-surface wind speed.

KEYWORDS: Turbulence; Oceanic waves; Surface observations; Empirical orthogonal functions; Statistical techniques

1. Introduction

Turbulence in the ocean surface boundary layer modulates the exchange of heat, momentum, and gases between the ocean and atmosphere. Our understanding of the chemical and energy balance across the air–sea interface is predicated on a careful accounting of turbulent dissipation rate $\epsilon(z)$ in the upper ocean (Belcher et al. 2012). While $\epsilon(z)$ often obeys classic "law of the wall" boundary layer scaling within the mixed layer and under steady wind forcing conditions [$\epsilon(z) \propto z^{-1}$], energetic surface processes such as wave breaking, Langmuir turbulence, and convective overturns can lead to strong near-surface (upper 1–10 m) enhancement and intermittency which is difficult to predict (Terray et al. 1996). For example, studies on the impact of breaking surface waves have shown $\epsilon(z)$ may increase as rapidly as z^{-2}, but a wide range of values have been reported (Gerbi et al. 2009; Thomson et al. 2016; Gemmrich 2010; Esters et al. 2018). Other processes can suppress near-surface mixing, such as diurnal surface heating (Sutherland and Melville 2015). An added difficulty lies in referencing stationary measurements to a moving sea surface (Thomson et al. 2016). Recent advances in the application of autonomous surface-following platforms have shown them to be a promising tool for measuring $\epsilon(z)$ in the very near surface under a wide range of forcing conditions (e.g., Thomson 2012; Grare et al. 2021; Hughes et al. 2021). However, instrument motion and strong wave orbital velocities often make it difficult to isolate turbulence in the surface-following reference frame. To that end, this manuscript provides an update

to the methodology employed by Thomson (2012) to estimate $\epsilon(z)$ from high-resolution (HR) acoustic Doppler current profiler (ADCP) data obtained with Surface Wave Instrument Floats with Tracking (SWIFTs). We seek to remove previously unaccounted for bias in the estimate of $\epsilon(z)$ due to platform motion and waves, as well as expand the application of our methodology to ADCP data collected from a Liquid Robotics SV3 Wave Glider (Thomson et al. 2018).

Estimates of dissipation rate have commonly been derived from ADCP data using Fourier analysis of high-frequency velocity time series due to past difficulty in achieving high-spatial-resolution measurements. That method requires the assumption of a steady background velocity which moves isotropic turbulence past the instrument, thereby converting time series to spatial series (the well-known "frozen-field" assumption). An advective velocity is particularly difficult to define in the near surface due to the presence of surface waves, strong wind driven shear and other energetic surface currents. Recent advancements in the application of pulse-to-pulse coherent methods of measuring velocity with ADCPs have enabled high-spatial-resolution velocity measurements ("HR" mode; Shcherbina et al. 2018), which can be used to estimate dissipation rate without needing to define an advective velocity (Gargett 1999). This is particularly advantageous for application to Lagrangian platforms, which are subject to significant wave-induced motion with respect to the water (Zippel et al. 2018).

Here we follow the structure function (SF) method of Wiles et al. (2006), which treats profiles of velocity as independent realizations of the spatial structure of turbulence, with no coherent relation to the profile observed before or after. The method

---

Corresponding author: Kristin Zeiden, kzeiden@uw.edu

consists of least squares fitting (LSF) the second-order velocity structure function $D(r)$ to a theoretical model derived from Taylor and Kolmogorov scaling theories, $D(r) \propto \epsilon r^{2/3}$. The model is assumed to be valid over some limited range of scales r within the inertial subrange. The SF method has typically been applied to velocity data obtained with bottom-mounted and moored ADCPs (e.g., Mohrholz et al. 2008; Lucas et al. 2014; Sutherland and Melville 2015; McMillan et al. 2016; Scannell et al. 2017; Guerra and Thomson 2017), while applications in the very near surface have been rarer. Gemmrich (2010) estimated $\epsilon(z)$ in the surface 1 m by applying the SF method to ADCP data collected from a ship-mounted frame. More recently, Thomson (2012), Thomson et al. (2016), and Zippel et al. (2018) used the SF method to estimate $\epsilon(z)$ in the surface 0.5 m from upward-looking pulse-coherent ADCPs mounted on SWIFT drifters.

The inherent challenge of the SF method is to isolate turbulence from nonturbulent velocities. Unlike Fourier spectral methods, which differentiate between these signals in frequency and wavenumber space, nonturbulent velocity gradients contribute to $D(r)$ at each scale. In the upper ocean, surface gravity waves are the most common source of bias. Recently, Scannell et al. (2017) introduced an analytic modification to the model of the inertial subrange structure function to account for wave bias. The authors demonstrated that the wave contribution goes as r^2, and can theoretically be separated from the turbulent component by introducing a third term in the model proportional to r^2. They validated this modified SF method using velocity data collected with ADCPs moored at ~20, 30, and 50 m depth, well outside the region of active wave breaking. No estimates were made close to the surface because the broadband ADCPs lacked the necessary resolution and their uplooking configuration caused strong acoustic reflections in the shallowest bins. The authors averaged over each 3-m profile to produce time series of ϵ at each ADCP depth. In the near surface, we are interested in resolving vertical structure as $\epsilon(z)$ can vary many orders of magnitude over a few meters (Thomson et al. 2016). Previous studies utilizing the SF method to estimate $\epsilon(z)$ using SWIFT drifters did not attempt to correct for bias due to surface waves (Thomson 2012; Thomson et al. 2016; Zippel et al. 2018). Zippel et al. (2018) used cross-spectra between velocity data and an onboard IMU to remove bias due to platform motion. However, the platform motion turns out to be a secondary concern in the SF method as the motion mostly affects time-domain calculations.

In this manuscript we present updates to the methodology used by Thomson (2012), Thomson et al. (2016), and Zippel et al. (2018) to compute dissipation from pulse-coherent HR ADCP data obtained in the near surface with SWIFT drifters. We refine the structure function algorithm, introduce a new method to account for bias due to nonturbulent shear, and expand the application to data collected with a surface-following SV3 Wave Glider. In contrast to previous SWIFT studies, the data used here are in a downward-looking orientation and span ~0.5–5 m depth. The increased profile range enables a clear picture of the impact of wave bias on the structure function in close proximity to the surface. Our updated methodology builds upon the method introduced by Scannell et al. (2017) to account for wave bias; however, we explore an alternative in

which low-mode wave profiles computed from empirical orthogonal functions (EOFs) of the data are removed prior to computing the structure functions. This new approach is motivated by our desire to resolve the vertical structure of dissipation rate, which we expect to predominantly follow law-of-the-wall scaling (z^{-1}), except close to the surface, where $\epsilon(z)$ may be impacted by wave effects. Resolving $\epsilon(z)$ necessitates small averaging windows and thus limits the number of points included in the least squares fit. Our results indicate that the empirical method of isolating turbulent velocity produces similar results to the analytic method introduced by Scannell et al. (2017), but with significantly reduced noise and lower mean-square percent error between the model and the data. Most importantly, these new dissipation estimates exhibit a clear dependence on near-surface wind speed over the broader SWIFT and Wave Glider datasets. This effect is heavily obscured by noise in the estimate obtained via the analytically modified SF method.

We begin with an overview of the inertial subrange structure function theory in section 2, followed by a description of the data in section 3. In section 4, we describe our methodology in detail using data from a single ADCP burst to illustrate. In section 5 we present detailed dissipation estimate results from that burst, and then apply our methodology to the broader mission data from both platforms. In section 6 we discuss the results and explore sensitivity to choices made in the processing. In section 7 we summarize and give recommendations for analysis.

2. Theory

In the absence of analytic descriptions of turbulence, oceanographers presently rely on a statistical model put forward by Taylor (1937) and Kolmogorov (1941). This model is predicated on the existence of an "inertial subrange" in which the rate of kinetic energy transfer between different scales of motion (ϵ) is a constant independent of scale and viscosity. From this assumption, Taylor used dimensional analysis to argue $\epsilon \propto u(r)^3 r^{-1}$ in the inertial subrange, where $u(r)$ is the characteristic velocity of turbulent eddies at scale r.

The method used to estimate $\epsilon(z)$ in this study relates Taylor's theoretical scaling to measurements of the second-order velocity structure function, $D(z, r) = \langle [u(z - r/2) - u(z + r/2)]^2 \rangle$, i.e., the ensemble-average squared velocity difference over a separation scale **r** centered at vertical position z. If the energy at depth z and scale r is predominately due to turbulent eddies, Taylor's scaling suggests

$$D(z, r) = C_\nu^2 \epsilon(z)^{2/3} r^{2/3}. \tag{1}$$

Here C_ν^2 is a constant empirically determined to be ~2.1 (Wiles et al. 2006). Dissipation rate can then be estimated by least squares fitting the observed velocity structure function at each depth to a linear function of the form

$$D(r) = Ar^{2/3} + N \tag{2}$$

and taking $\epsilon(z) = [A(z)/C_\nu^2]^{3/2}$. The model intercept N gives the uncertainty in u^2, assumed to be proportional to the instrument noise at each depth.

This model of inertial subrange turbulence holds approximately in the deep ocean away from boundaries and in the presence a steady mean flow, but near the surface there are likely high-frequency, nonturbulent velocity gradients which contribute to D. The most likely source of bias is energetic surface gravity waves with small vertical decay scales (i.e., short waves). Waves may also indirectly contribute to bias if the wave-induced platform motion is significant in the presence of otherwise steady background shear. Scannell et al. (2017) recently developed an analytic framework to account for wave bias in $D(r)$: if nonturbulent velocity gradients are sufficiently linear on the spatial scales of interest, their contribution to the structure function will go as r^2. This modified model of the structure function accounts for both turbulent and nonturbulent contributions by the addition of a third term:

$$D(r) = Ar^{2/3} + B(r^{2/3})^3 + N. \qquad (3)$$

The original relationship between ϵ and A is preserved, and $\epsilon(z)$ may be determined in the same fashion by fitting the observed $D(r)$ to Eq. (3) at each depth.

3. Data

To demonstrate the robustness of the SF method of estimating turbulence from ADCP data collected in a surface-following reference frame, we apply the method to data obtained with two different platforms: SWIFTs (Thomson 2012) and a Liquid Robotics SV3 Wave Glider (Hine et al. 2009; Thomson et al. 2018). The SWIFTs and Wave Glider were equipped with the same ADCPs (Nortek Signature 1000), but operated under very different environmental conditions. The SWIFTs were deployed in the Southern California Bight in late March 2017 during the Office of Naval Research "Langmuir Circulation" Departmental Research Initiative (LC-DRI) field experiment. The Wave Glider was deployed in the Southern Ocean in November 2019 during a 4-month survey of the Antarctic Circumpolar Current fronts within Drake Passage. We apply our methodology to subsets of the data collected away from strong fronts and during periods with near-surface wind speeds less than 15 ms^{-1}, such that we expect dissipation rates to be primarily a function of wind speed.

a. ADCP configuration

The Nortek Signature 1000 has four slanted beams operating in broadband mode, and a fifth vertical beam which operates in an interleaving pulse-coherent HR mode (Figs. 1a,c). Only the fifth beam is used to compute dissipation rate, so we do not discuss the broadband data further in this manuscript. In HR mode, a pair of coherent short pulses separated by a lag time much longer than the pulse duration is emitted each ping (a "pulse pair"). Along-beam velocity is then a function of the phase of the complex correlation of the pulse-pair echo, lag time, the carrier frequency of the pulses, and the local sound speed [Eq. (1) in Shcherbina et al. 2018]. Although the precise temporal and spatial resolution is user defined, HR mode is designed to produce profiles of along-beam velocity with bin sizes of a few centimeters at frequencies greater than 1 Hz. For this study, ADCPs on both platforms
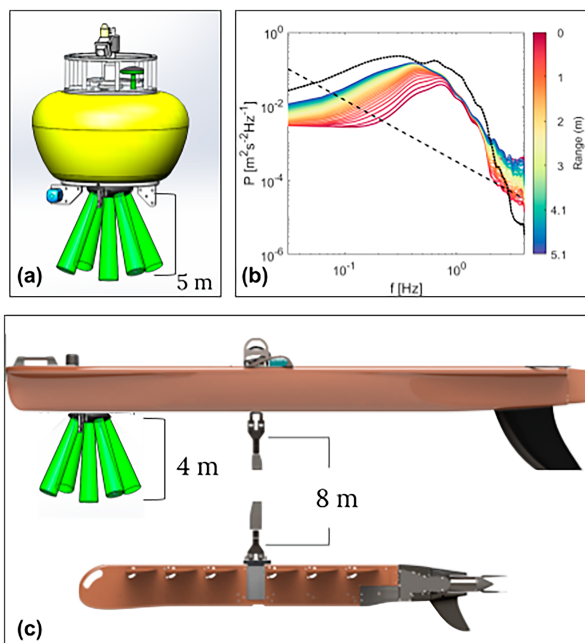

FIG. 1. Instrument schematics for the (a) SWIFT drifters and (c) Liquid Robotics SV3 Wave Glider, as well as (b) along-beam velocity frequency spectra computed from a single 8-min burst of data obtained from a SWIFT-mounted Signature 1000 ADCP. Profile ranges were 5.12 and 3.84 m on the SWIFT and SV3, respectively. ADCP depth bins were 0.04 m on both platforms. Velocity frequency spectra in (b) are colored by range from the transducer (red colors are closer), and the black dotted curve shows the spectra of the instrument vertical velocity (i.e., platform motion). The black dashed line gives an example theoretical slope for turbulent velocity spectra, here corresponding to $\epsilon = 10^{-4}$ m^2 s^{-3} and assuming an advective velocity of 0.25 m s^{-1} (the drift velocity of the SWIFT). Velocity variance at all depths is dominated by a broadband peak around 0.5 Hz due to surface gravity waves and instrument noise dominates frequencies greater than 1 Hz. Energy increases with distance from the transducer because velocity here is relative to the ADCP/SWIFT motion.

were configured to sample in 0.04 m bins at 8 Hz over 8-min "bursts" (Table 1). The range of the center beam in HR mode was 5.12 m as configured on the SWIFTs, and 3.84 m on the Wave Glider. The depth of the transducer on both platforms was 0.2 m. Combined with a blanking distance of 0.1 m, the effective depth ranges of the ADCPs were 0.3–5.42 m and 4.14 m on the SWIFTs and Wave Glider, respectively. The ADCPs on board the SWIFTs were configured to burst sample every 12 min. The ADCP on board the Wave Glider was configured to burst sample at the top of every hour.

Prior to analysis, velocity data were quality controlled by removing velocity spikes which occur due to phase ambiguity inherent in the pulse-pair coherence method of determining velocity (Shcherbina et al. 2018). Spikes are identified in each ping using a threshold maximum deviance from a 1-m median filtered profile, and compose anywhere from 10% to 80% of the data depending on the environmental conditions (i.e., high- or low-scattering environments). In addition to removing individual data spikes, entire pings are removed if the standard

TABLE 1. ADCP configurations as deployed on the SWIFTs and Liquid Robotics SV3 Wave Glider.

Signature 1000 burst sampling configurations					
Platform	Bin size (m)	Range (m)	Depth (m)	Rate Hz)	Duration (min)
SWIFT	0.04	5.12	0.2	8	8
Wave Glider	0.04	3.84	0.2	8	8

deviation of the filtered velocity profile exceeds 0.01 m s^{-1}, typically a symptom of excessive spiking. Additional details of the despiking routine are given in appendix A.

b. Example data

An example 2 min of quality-controlled ADCP data from a single 8-min burst obtained from a SWIFT drifter is given in Fig. 2. Instrument orientation (pitch and roll), acoustic backscatter amplitude and pulse-pair correlation are shown in addition to the along-beam velocity. The tilt of the instrument varies up to 30°, but with a standard deviation angle from the vertical of just 10° (Fig. 2a). Corresponding vertical displacements are 1 m at the base of the profile, though we note this does not affect the along-beam bin spacing. Acoustic backscatter amplitude is highest near the transducer and characterized by strong intermittency every ~20–30 s (Fig. 2b). Weaker pulses in amplitude with a period of about 1 s are due to the SWIFT bobbing at its natural frequency. Pulse-pair echo correlation is 85% on average, but randomly drops below 50% over an entire profile (Fig. 2c). Pings with correlation dropout are typically characterized by a high percentage of data spikes and are discarded in our despiking routine (appendix A). In this example 10% of all pings in the burst are discarded. Along-beam velocity is $O(0.1)$ m s^{-1} due to a combination of waves and instrument bobbing (Fig. 2d). However, a simple 1-m

moving Hann window filter applied to each velocity profile reveals clear fine-scale structure in the data (Fig. 2e). The high-passed velocity is $O(0.01)$ m s^{-1}, an order of magnitude weaker than the ambient waves.

Velocity frequency spectra computed from the example burst data are dominated by waves, platform motion, and noise (Fig. 1b). Spectra are plotted as a function of range from the transducer (colored lines), and the spectrum of vertical instrument velocity obtained from an onboard inertial motion unit is overlaid in black (i.e., platform motion). Spectra at each depth are dominated by a broadband peak from 0.1 to 1 Hz due to surface gravity waves. Because velocities measured by the ADCP are relative to the motion of the SWIFT, energy increases with distance from the transducer due to wave shear. This depth dependence disappears around 1 Hz, the natural frequency of the SWIFT, as vertical platform motion with respect to the water (i.e., bobbing) introduces a strong relative velocity independent of distance from the transducer. We note that the use of frequency spectra to estimate dissipation rate would require both the removal of wave velocities from the data and an accurate characterization of an advective velocity for each depth bin. However, even if wave velocities could be fully characterized, the ping-to-ping horizontal and vertical displacement of each ADCP bin due to the strong platform motion (up to 1 m at the base of the profile)
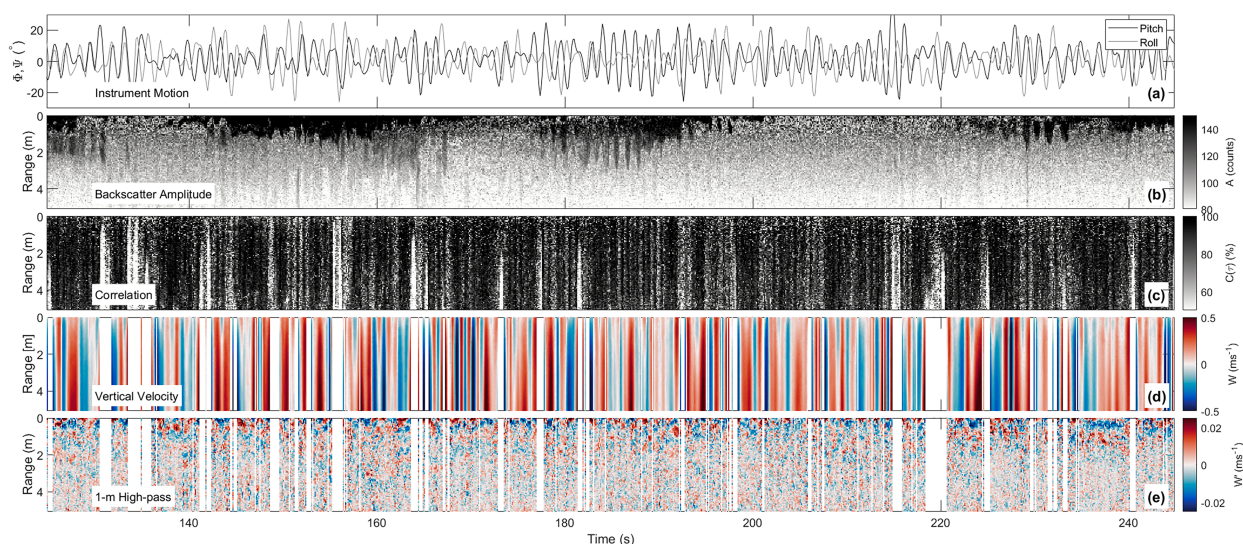

FIG. 2. Example ADCP data collected from a SWIFT drifter. Shown are (a) instrument pitch and roll, (b) backscatter amplitude, (c) pulse-pair correlation, (d) along-beam velocity, and (e) 1-m high-passed along-beam velocity. The velocity data have been despiked (appendix A). Surface gravity waves and the bobbing of the SWIFT at its natural frequency dominate the along-beam velocity variance, but fine-scale structure is evident in the high-passed data. Only 2 min of the 8-min burst are shown here for clarity.

likely violates the coherence of the turbulent velocity observations in time. This motivates treating velocity profiles as independent spatial measures of the turbulence, rather than as temporal data. We discuss problems with using spectral methods further in appendix B.

4. Methodology

In this section we provide a detailed description of the methodology used to compute $\epsilon(z)$ from HR pulse-coherent ADCP velocity data, using the example burst data shown above to illustrate. We begin by computing EOFs of the data, which we use to filter out wave orbital motions. We demonstrate that a few of the most energetic EOFs have characteristics of surface gravity waves, while the weaker EOFs have characteristics of inertial subrange turbulence. We then describe the algorithm used to compute the second-order velocity structure functions at each depth and compare characteristics of structure functions derived from the unfiltered velocity, EOF filtered velocity, and a spatial high-pass filtered velocity. We follow with details of the least squares fitting algorithm, and present quality metrics available to assess the validity of the subsequent dissipation rate estimates.

a. Empirical wave filtering

As described in section 2, nonturbulent wave orbital velocities can contribute substantially to the total observed shear near the surface and create bias in dissipation rates estimated from the velocity structure function. Here we describe a method to separate wave orbital velocities from the turbulent signal using EOFs of the data. EOF analysis can be a useful tool to describe the dominant statistical patterns of variability within a set of observations (Hannachi et al. 2007). The primary goal of EOF analysis is to reduce the data into a few "modes" that contain a bulk of the observed variance. EOFs are eigenvectors ($\mathbf{E}$) of the data–data covariance matrix ($\mathbf{C}$) with corresponding eigenvalues (e) defined by the familiar eigenvector equation

$$\mathbf{C}\mathbf{E}_i = e_i\mathbf{E}_i, \tag{4}$$

where $i = 1 \ldots N$, the number of data vectors (each of equal length M). Here, the data are the vertical velocities obtained each during each ADCP burst, an $N \times M$ matrix $\mathbf{W}'$, such that N is the number of ADCP bins and M is the number of pings. A time-mean velocity profile ($\mathbf{W}_0$, $N \times 1$) is removed from the data prior to computing the covariances (i.e., $\mathbf{W}' = \mathbf{W} - \mathbf{W}_0$). Thus, $\mathbf{C}$ is the $N \times N$ matrix of temporal covariances between all possible ADCP bin pairs, with N associated eigenvectors ($\mathbf{E}_i$) and eigenvalues (e_i). For each EOF, $\mathbf{E}_i$ is an $N \times 1$ unit vector giving relative magnitude at each vertical position, and e_i is a scalar giving the fractional variance of the data contained in that EOF. Because $\mathbf{C}$ is symmetric, the $\mathbf{E}_i$ are orthogonal. Finally, the time-varying amplitude (α_i) of each EOF can be obtained by projecting $\mathbf{E}_i$ back onto the original velocity data,

$$\alpha_i = \mathbf{E}_i^{\mathsf{T}}\mathbf{W}', \tag{5}$$
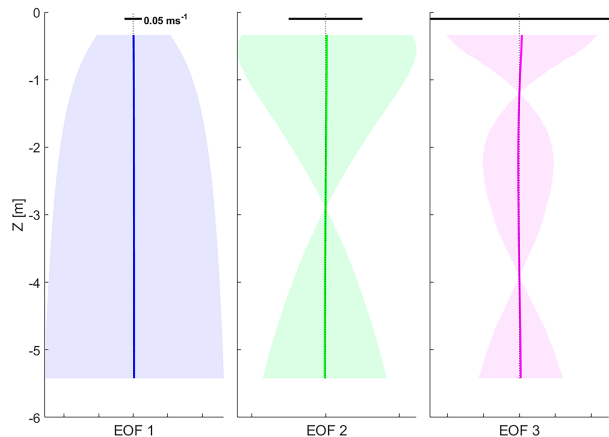
and the original data may be reconstructed from the EOFs as

FIG. 3. Three most energetic EOFs of along-beam velocity computed from the example burst velocity data (Fig. 2). Shaded regions indicate standard deviation of the EOF at each depth. The black horizontal bar in each plot is equal to 0.05 m s^{-1} to show the different absolute magnitudes of the EOFs (note the change across each plot).

$$\mathbf{W} = \sum_{i=1}^{N} \mathbf{E}_i\alpha_i + \mathbf{W}_0. \tag{6}$$

From Eq. (6) it is clear that EOF analysis restructures the data as a linear superposition of vertical modes with time varying amplitude. For example, the vertical structure and variance of the three most energetic EOFs of the example burst velocity data (section 3) are shown in Fig. 3. These EOFs resemble low-mode harmonics with no, one, and two zero crossings. Subsets of EOFs can be used to reconstruct specific features of interest in the data. We emphasize that EOFs are statistical, rather than true physical, modes and that they are orthogonal by definition. We discuss subsequent strengths and limitations of the EOF decomposition in section 6b.

Full inspection of all EOFs of the example burst data reveal the most energetic EOFs have characteristics expected of surface gravity waves, while all lower energy EOFs have characteristics of inertial subrange turbulence (Fig. 4). The first EOF contains 97% of the velocity variance ($e_1 = 0.97$). As noted above, its eigenvector ($\mathbf{E}_1$) is a profile with no zero crossings and elevated shear near the surface (blue lines in Figs. 3 and 4a). The power spectrum of its time varying amplitude (α_1) is dominated by a broadband peak from 0.1 to 1 Hz, consistent with motion spectra obtained from the onboard IMU (Fig. 4c). As expected for surface gravity waves, the vertical wavenumber spectrum of the first EOF has a strong peak at the lowest wavenumbers and very little comparative energy at wavenumbers higher than ~ 1 m^{-1} (Fig. 4d). The second and third EOFs are similarly low mode, with one and two zero crossings, and their frequency spectra are dominated by energy in the wave band (green and magenta lines, respectively, in Figs. 3 and 4). In contrast to these first three EOFs, frequency spectra of all subsequent EOFs are comparatively flat with no peaks in the wave band (yellow–purple gradient colors in Fig. 4). Their vertical
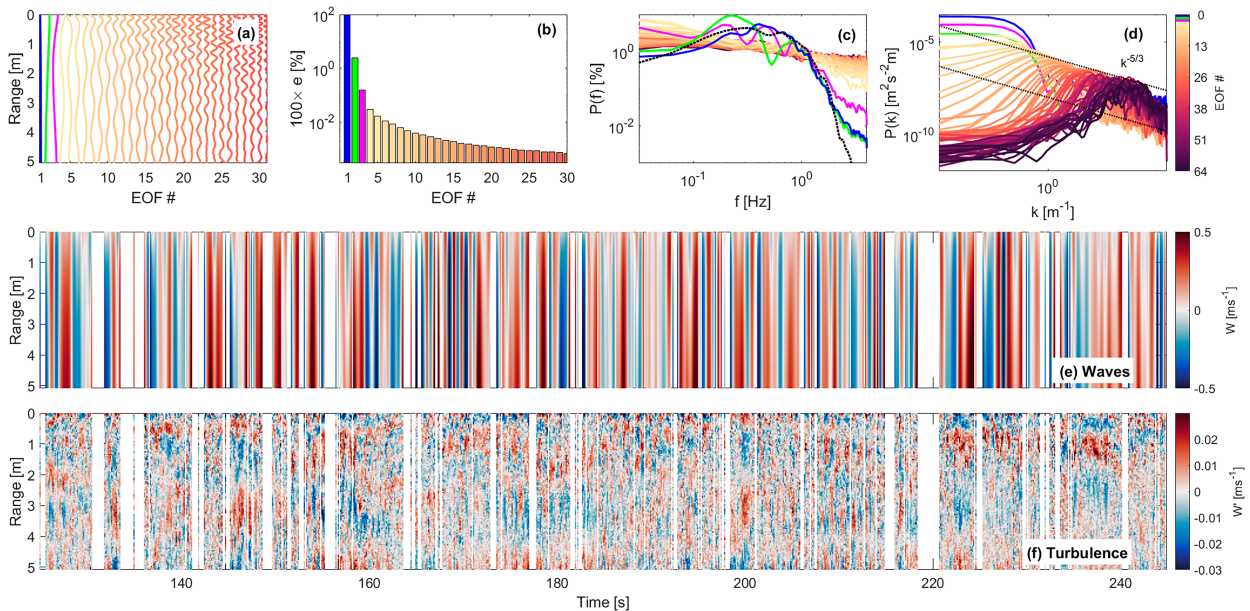
FIG. 4. Empirical orthogonal functions (EOFs) of the example burst data. Shown are the (a) EOF eigenvectors, (b) percent velocity variance described by each EOF, (c) power spectral density of the time varying amplitude of each EOF, and (d) and wavenumber spectra of each EOF. In (a) and (b) and and (c) and (d) only the first 30 and 64 EOFs are shown for clarity, respectively. The black dotted line in (c) is the instrument motion spectra, as in Fig. 1b. The first three EOFs have characteristics of surface gravity waves, with low vertical wavenumbers and broadband frequency peaks in the wave band [blue, green, and magenta bars and lines in (a)–(d)]. Subsequent EOFs have relatively flat frequency spectra, and broadband peaks in wavenumber spectra at progressively higher wavenumbers as their energy decreases. The slope produced by these descending peaks corresponds to $k^{-5/3}$, consistent with inertial subrange turbulence. The first three EOFs are used to reconstruct (e) wave profiles, which are then removed from the data to reveal (f) the EOF-filtered turbulent velocity.

wavenumber spectra are dominated by broadband peaks at progressively higher wavenumbers, consistent with an increasing number of zero crossings in each eigenvector. A striking feature of these higher-mode EOFs is that their energy decreases as $\sim k^{-5/3}$, a hallmark of inertial subrange turbulence (black dashed lines in Fig. 4d).

We proceed to construct empirical wave profiles using the first three EOFs, which have characteristics of surface gravity waves (we explore sensitivity of our results to this choice in section 6b). The reconstruction is achieved by multiplying the eigenvectors of these EOFs by their time varying amplitudes and adding them together [Eq. (6), only using $i = 1{:}3$]. The resultant wave profiles are then subtracted from the data to isolate the turbulent component of velocity (Figs. 4e,f, respectively). Turbulent velocities are $O(0.01)$ m s^{-1}, with coherent structures of variable size which persist up to tens of seconds.

It is evident that removing the low-mode empirical wave profiles from the data is similar in effect to performing a spatial high-pass filter. Figure 5 compares the two methods of filtering using an example profile. The two filtered velocity profiles exhibit the same fluctuations at small scales, but there are $O(1)$ m gradients present in the EOF-filtered velocity (red; w^*), which were removed by the high-pass spatial filter (cyan; w^+), particularly near the surface. As will be shown in the next section, this means the spatial filter places an upper limit on the separation scales used to fit the velocity structure function to Eq. (2).

b. Ensemble-average structure functions

Here we provide a general description of how an "ensemble-averaged" second-order velocity structure function $D(r)$ is computed from velocity data. This algorithm applies to all versions of velocity, filtered or unfiltered. The first step in the process is to generate an $N \times N$ matrix $\delta\mathbf{W}_j$ of velocity differences between all possible data-pair combinations from each of the M velocity profiles. Here M is the number of pings in the ensemble (i.e., burst) and $j = 1 \dots M$. As in section 4a, N is the number of ADCP range bins. If each velocity profile is an $N \times 1$ vector $\mathbf{w}_j$, then $\delta\mathbf{W}_j = (\mathbf{w}_j - \mathbf{w}'_j)$, an $N \times N$ antisymmetric matrix. We attempt to account for any data spikes which have not been filtered during the initial QC process by removing points from the ensemble outside five standard deviations from the mean of the distribution (i.e., standard deviation in $\delta\mathbf{W}_j$ along the M dimension). The separation scale and mean vertical position of each data pair in $\delta\mathbf{W}_j$ are given by the $N \times N$ matrices $\mathbf{R} = \mathbf{z} - \mathbf{z}'$ and $\mathbf{Z} = (\mathbf{z} + \mathbf{z}')/2$, respectively, where $\mathbf{z}$ is the $N \times 1$ vector of ADCP bin depths. Next, a single $N \times N$ burst-averaged structure function matrix is obtained by taking the mean over the ensemble of $\delta\mathbf{W}_j^2$, i.e., $\mathbf{D}(\mathbf{z}, \mathbf{r}) = (1/M)\sum_{j=1}^{M} \delta\mathbf{W}_j^2$. Note that while $\delta\mathbf{W}_j$ are antisymmetric, the squaring of $\delta\mathbf{W}_j$ implies $\mathbf{D}(\mathbf{z}, \mathbf{r})$ is a symmetric matrix. Finally, $\mathbf{Z}$ is used to bin $\mathbf{D}(\mathbf{z}, \mathbf{r})$ and $\mathbf{R}$ to the original ADCP bin depths. This step yields a structure function vector $\mathbf{D}(\mathbf{r})$ and scale vector $\mathbf{r}$ at each depth in the profile. Hereafter, we drop the explicit dependence on $\mathbf{r}$ from
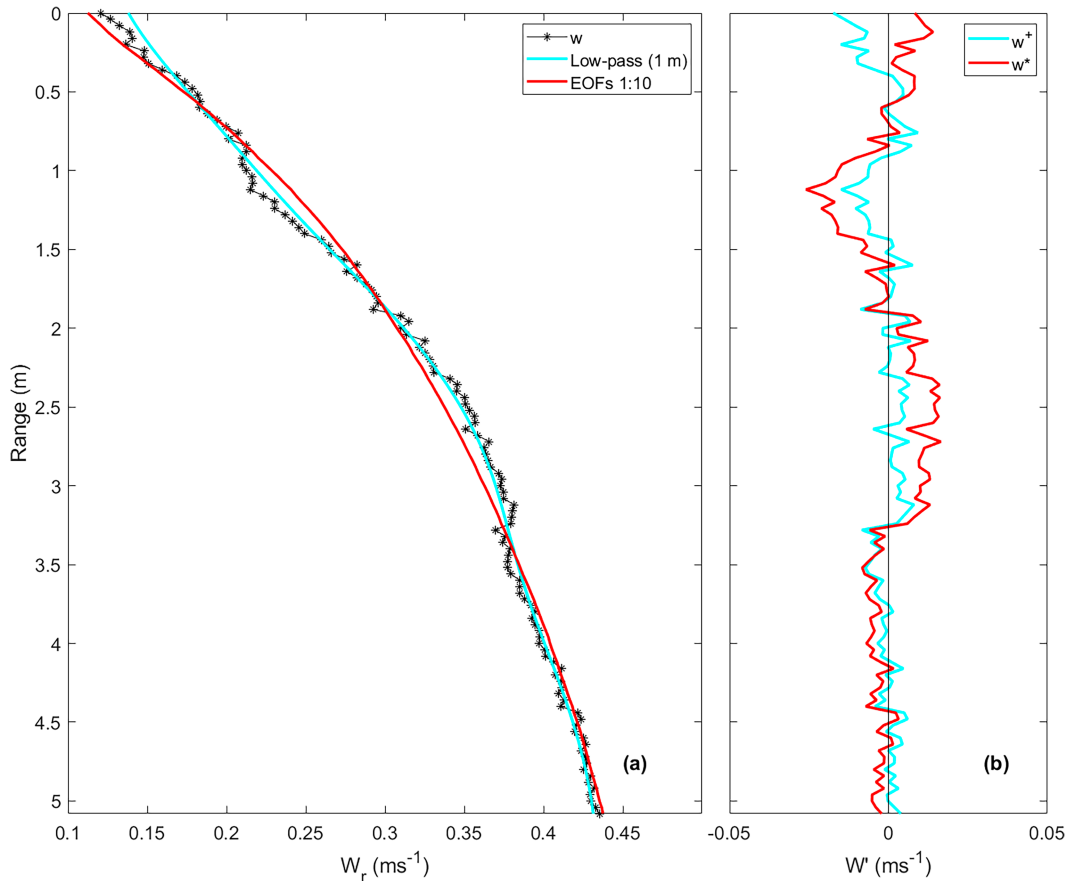
FIG. 5. (a) Example velocity profile produced by a single ADCP ping compared with a 1 m smoothed profile and the empirical wave profile computed from the first three EOFs of the example burst data (black, cyan, and red lines, respectively) and (b) the corresponding high-pass and EOF-filtered velocity profiles for this ping. Differences between the two methods of filtering are strongest near the surface, where the spatial high-pass filter underestimates the near-surface shear of the wave.

the notation, simply using **D** to signify the (vector) structure functions used to estimate dissipation rate at each depth.

Consistent with the $k^{-5/3}$ wavenumber distribution of the turbulent EOFs, structure functions derived from the EOF-filtered velocity (denoted $D*$) increase with separation scale as $\sim r^{2/3}$ up to 1 m, where they exhibit local maxima (Fig. 6a). The maxima may reflect an upper limit to the inertial subrange, but is likely impacted by our choice of which EOFs to remove when isolating $w*$. Velocities $D*$ are overall strongest near the surface and decrease with depth; $D*$ in the shallowest few bins have slopes slightly steeper than $r^{2/3}$. At the maximum possible separation scale at each depth, $D*$ are much steeper than $r^{2/3}$. These scales necessarily include the ADCP bins closest to the transducer. It is possible those bins contain instrument noise which has not been adequately filtered by our despiking routine or that they retain some wave shear. Alternatively, near-surface turbulence may not conform to the isotropic assumptions of Kolmogorov theory. Structure functions derived from the high-pass filtered velocity (denoted D^+) are similar to $D*$ (Fig. 6b). D^+ exhibit an $r^{2/3}$ dependence at fine scales, decrease in magnitude with depth and increase rapidly at the greatest separation scales. However,

D^+ have a uniform local maxima at $r = 0.5$ m, which has been imposed by the spatial filter.

Structure functions computed from the unfiltered velocity (denoted D) exhibit no local maxima and are steeper than $r^{2/3}$ throughout, but with similar overall depth dependence to the prefiltered velocity structure functions (Fig. 6c). Slopes of D are slightly steeper than $r^{2/3}$ at small separation scales and approach r^2 with increasing scale (black dashed line) as predicted by Scannell et al. (2017). In theory, D is expected to be a linear combination of these two components at all scales, and thus separable by applying Eq. (3) in lieu of Eq. (2). However, the similarity between r^2 and $r^{2/3}$ at fine scales emphasized by Fig. 6c foreshadows limitations on the application of Eq. (3) when using small fitting ranges.

The divergence of $D*$ and D^+ from $r^{2/3}$ at separation scales of ~ 1 and 0.5 m, respectively, emphasizes the importance of limiting the range of scales included in the least squares fit. Including scales which are too large will likely result in an underestimate of the dissipation due to the decreased slope in $D*$ and D^+ induced by their local maxima. Further, a major strength of the structure function method is the ability to
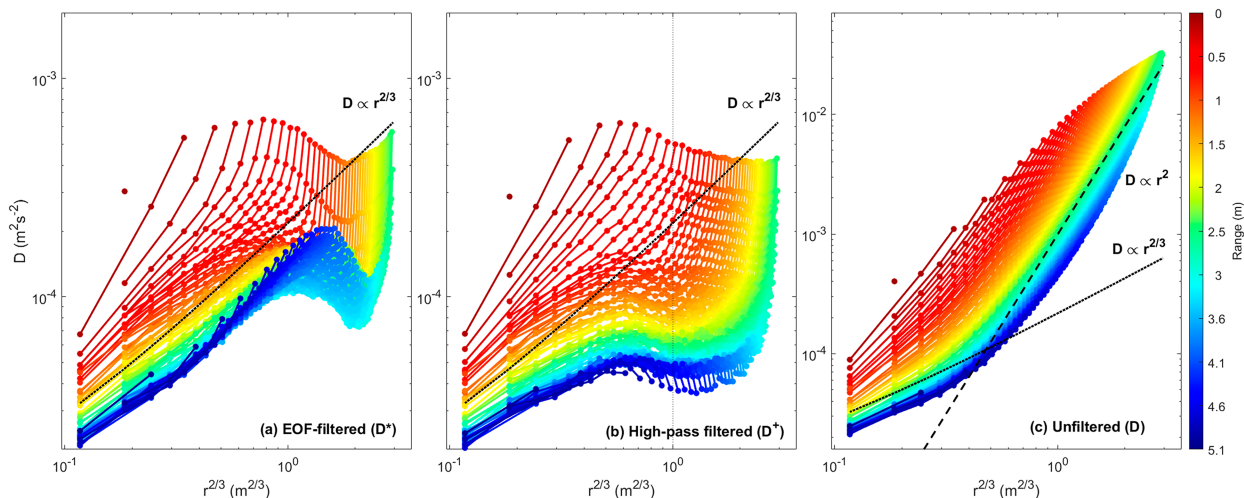
FIG. 6. Second-order velocity structure functions $\mathbf{D(r)}$ plotted against separation scale (here given as $r^{2/3}$) as computed from the (a) EOF-filtered velocity (D^*), (b) 1 m high-pass filtered velocity (D^+), and (c) unfiltered velocity (D), colored by range from the ADCP transducer (i.e., depth bin). The two filtered velocity structure functions are very nearly proportional to $r^{2/3}$ at small separation scales, while the full velocity structure function is steeper than $r^{2/3}$, approaching r^2 beyond $r = 1$ m.

obtain localized estimates of dissipation rate. An increase in the separation scale at any depth necessarily reduces vertical resolution, and risks performing the LSF over a range in which ϵ is not uniform. This is especially important close to the ocean surface, where vertical gradients in dissipation are expected to be strongest. The reason to consider including greater separation scales when fitting Eq. (2) or Eq. (3) to the structure function is to reduce error in the fit (by increasing the number of points). The impact of varying the maximum separation scale used in the LSF is explored in section 6c.

c. Least squares estimate of dissipation rate

As described in section 2, we compute profiles of dissipation from each ADCP burst by least squares fitting the structure function at a given depth to the model $D = Ar^{2/3} + N$ [Eq. (2)], with an option to include a third term to account for nonturbulent wave orbital shear analytically [Br^2 in Eq. (3)]. The fit is performed over positive r only, as the structure function is the same for positive and negative separation scales. The LSF should be limited to a range of scales assumed to be within the inertial subrange, but the practical considerations described in the previous section suggest stricter limits are likely necessary. A least squares estimate of dissipation within each depth bin is then given by $\epsilon = (A/C_\nu^2)^{3/2}$, where C_ν^2 is a constant empirically determined to be ~ 2.1 (Wiles et al. 2006).

A consideration when performing the LSF is the effective resolution of the resulting dissipation rate profile. The resolution is in part dictated by the size of the depth bins used to convert the matrix $\mathbf{D(z, r)}$ into N vectors $\mathbf{D(r)}$ (see previous section). This is not to be confused with the choice of fitting range (i.e., which r are used in the LSF at each depth), although both will impact the resolution of the profile. Here we use vertical bins which correspond to the original ADCP bin size in an effort to preserve the vertical resolution of the

velocity data, and limit the LSF fitting range to $r \leq 0.16$ m. This means there are four points included in the fit at each depth. Our choice of fitting range is somewhat arbitrary, except that visual inspection of the structure functions (Fig. 6) suggests they deviate from the Kolmogorov model at higher separation scales. Four points provide an overdetermined fit to Eq. (2), and thus an estimate of the MSPE. When least squares fitting D to Eq. (3), we increase the fitting range to $r \leq 0.24$ m to account for the additional degree of freedom in the modified model. This maintains the same proportion of data to unknowns as when using Eq. (2). We explore the impact of varying r_{max} in section 6c.

d. Quality metrics

To help gauge the validity of each dissipation rate estimate we compute three quality metrics. The first is a best-fit power law to the velocity structure function, $D \propto r^n$. The power law is obtained by performing a linear regression on the logarithms of r and D [i.e., on $\log(D) = n\log(r)$ to obtain n]. This metric (n) is used to evaluate how closely the observed structure function conforms to the Kolmogorov model [Eq. (2)], in which $n = 2/3$. The second metric is the estimate of ADCP noise given by the second term in Eq. (2), $N = 2\sigma_N^2$. We expect σ_N^2 to be no greater than the a posteriori estimate derived by Shcherbina et al. (2018), which is proportional to the inverse pulse-pair correlation squared [their Eq. (11), denoted here as σ_{S18}^2]. The third quality metric is the mean-square percent error (MSPE) of the LSF to Eq. (2), given by

$$\text{MSPE} = \left\langle \left[\frac{d_m - d}{d_m}\right]^2 \right\rangle \qquad (7)$$

at each depth. Here d and d_m are the observed data used in the LSF and the subsequent model data, respectively. The angle

TABLE 2. Lookup table of the different symbols used to describe $\epsilon(z)$ estimates obtained via the different processing methods described in section 4.

Symbol	Name	Method
	Summary of dissipation rate estimate versions	
ϵ	Unfiltered	LSF Eq. (2) to unfiltered velocity SF (D, derived from w)
ϵ^*	EOF filtered	LSF Eq. (2) to EOF-filtered velocity SF (D^*, derived from w^*)
ϵ^+	High-pass filtered	LSF Eq. (2) to HP-filtered velocity SF (D^+, derived from w^+)
ϵ'	Analytic	LSF Eq. (3) to unfiltered velocity SF (D, derived from w)

brackets indicate an average over all points in the fit. When ϵ is computed using the analytically modified model [Eq. (3)] these quality metrics are computed after first removing the resultant shear term (Br^2) from D, and then refitting the Kolmogorov model [Eq. (2)] to the residual, i.e., to $D' = D - Br^2$.

5. Results

In this section we present dissipation rate profiles obtained via the methodology described in section 4. First, we examine detailed results from the example burst, comparing four different estimates of $\epsilon(z)$. The first three estimates are obtained by least squares fitting the classic Kolmogorov model [Eq. (2)] to the unfiltered, EOF-filtered, and high-pass filtered velocity SFs (denoted ϵ, ϵ^*, and ϵ^+, respectively). We expect ϵ to be biased due to the retained wave orbital velocities in D. The fourth estimate is obtained by least squares fitting the

analytically modified SF model [Eq. (3)] to the unfiltered velocity SF (denoted ϵ'). Table 2 summarizes the different versions of dissipation rate and how they were calculated. We follow this detailed examination with dissipation rate estimates from the broader SWIFT and Wave Glider datasets.

a. Profiles of dissipation rate

Profiles of dissipation rate computed by fitting the Kolmogorov model [Eq. (2)] to the two filtered velocity SFs are in close agreement; ϵ^* and ϵ^+ decay in proportion to z^{-1}, as predicted by classic law-of-the-wall scaling (red and cyan lines in Fig. 7a). Values decrease from $\sim 10^{-5}$ m^2 s^{-3} at 1 m to $\sim 5 \times 10^{-7}$ m^2 s^{-3} at 5 m depth. Above 1 m, ϵ^* and ϵ^+ decay more rapidly than z^{-1} away from the surface, increasingly precipitously by an order of magnitude in the shallowest five bins. In comparison to these estimates, ϵ computed by fitting Eq. (2) to the unfiltered velocity SF is biased high, as expected due to the contribution from wave
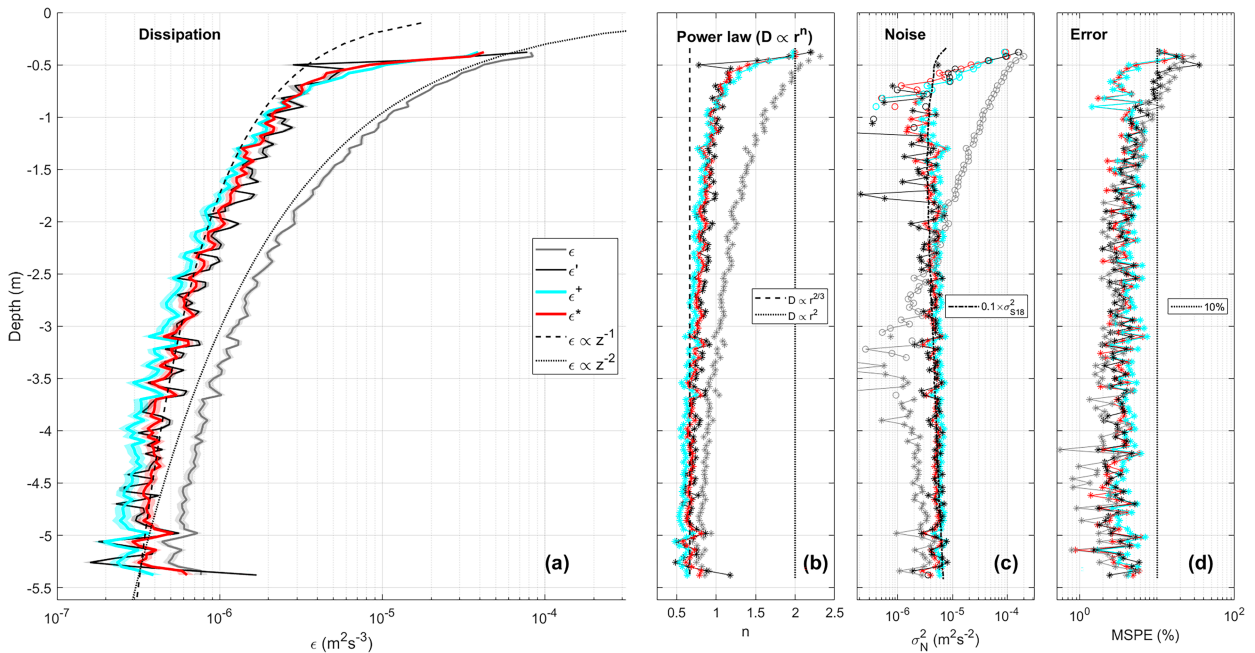

FIG. 7. (a) Profiles of dissipation rate obtained from least squares fitting the EOF-filtered, high-pass filtered, and unfiltered velocity structure functions to Eq. (2) (red, cyan, and gray lines), as well as the unfiltered velocity structure function to Eq. (3) (black line). For comparison, the thin dashed and dotted black lines in (a) are curves corresponding to $\epsilon \propto z^{-1}$ and z^{-2}, respectively. Also shown are the corresponding quality metrics: (b) the best-fit power law to each structure function, (c) the estimate of ADCP noise given by the fit, and (d) the mean-square percent error (MSPE) of the fit. In (c), the absolute value of the ADCP noise estimate is plotted to avoid the problem of taking a logarithm of a negative value, but negative values are indicated with open circles.
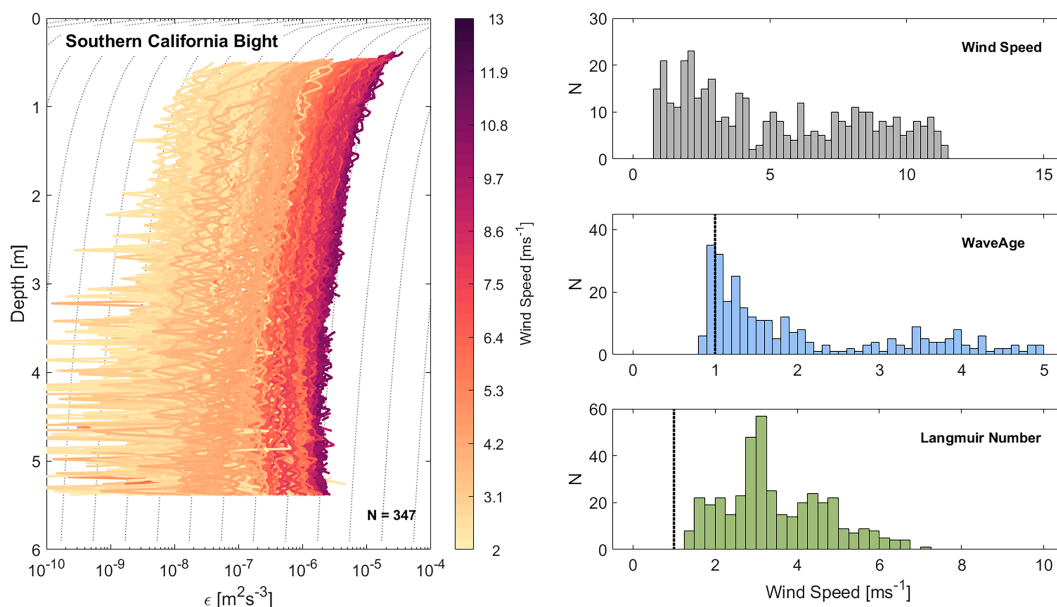
FIG. 8. Profiles of dissipation rate obtained by applying the SF method to EOF-filtered velocity data obtained from SWIFT drifters in the Southern California Bight in March and April of 2017. Profiles of ϵ are colored by 1 m wind speed. Gray dotted lines show $\epsilon \propto z^{-1}$. The forcing conditions during the observation period are summarized by histograms of wind speed (gray), wave age (blue), and Langmuir number (green).

shear (gray line). The wave-biased estimate also decays more rapidly than the filtered estimates, approximately z^{-2} over the entire profile. Dissipation rate computed by fitting the analytically modified SF model [Eq. (3)] to the unfiltered velocity ϵ' appears to be unbiased and in close agreement with ϵ^+ and ϵ^*, although with discernibly greater along-beam variance (black line).

At depths greater than 1 m, the best-fit power laws to D^*, D^+, and D' are all very nearly $r^{2/3}$. Corresponding estimates of ADCP noise from the LSF are an order of magnitude weaker than predicted by σ_{S18}^2, but increase with depth in proportion to the inverse burst-mean pulse-pair correlation squared as expected (black dashed line in Fig. 7c). The adherence of these metrics to their expected values is quantitatively reflected in the low MSPE of the LSF to D^*, D^+, and D', which is less than 10% below 1 m depth. The three quality metrics suggest our estimates of ϵ from all three methods are unbiased below 1 m.

Above 1 m, the quality metrics suggest all versions of ϵ are unreliable. The best-fit power laws to D^* and D^+ rapidly increase toward the surface, approaching r^2. These steep SF gradients generate large, nonphysical, negative estimates of the ADCP noise in the LSF (empty circles Fig. 7). MSPE increases rapidly above 0.5 m, but only exceeds 10% in the shallowest four depth bins. The convergence of ϵ^* and ϵ^+ and their corresponding quality metrics in the upper 1 m to the values given by fitting the wave-biased D to Eq. (2) suggests that retained wave shear may be contributing to bias at depths shallower than 1 m. However, this inference is at odds with the results of applying the modified SF method, which we expect to account for wave shear. Instead, the best-fit power law to D' also increases rapidly from $r^{2/3}$ to r^2, the corresponding ADCP noise estimate is

negative, and the MSPE exceeds 10%. These characteristics suggest that the near-surface bias in ϵ is either due to poor ADCP quality close to the transducer, or that turbulence observed in this depth range does not support the statistical assumptions of Kolmogorov theory.

b. Application to SWIFT and Wave Glider datasets

Application of the structure function methodology to the broader SWIFT and Wave Glider datasets reveals a clear relationship between dissipation rate and near-surface wind speed (Figs. 8 and 9). Shown in each are ϵ^* derived from the EOF filtered velocity, colored by 1 m wind speed. As in the example burst, the three most energetic EOFs of each burst have been used to construct a wave profile which is removed from the data. Here we have quality controlled the dissipation rate estimates by applying a maximum allowed MSPE of 10%. The primary consequence of this threshold is to remove bins in the very near surface, although the precise depth above which the dissipation rates become unreliable varies across individual profiles. In total there are 347 profiles from the SWIFTs and 388 profiles from the Wave Glider.

In both datasets, dissipation rate increases in magnitude with increasing wind speed and profiles follow $\sim z^{-1}$, except very close to the surface ($z < 1$ m) where the profiles are steeper. When referring to vertical profiles, by "steeper" we mean has a stronger gradient in the vertical. This is clearest at wind speeds greater than ~ 5 m s^{-1}. Wind speeds ranged from 1 to 12 ms^{-1} in the Southern California Bight, and corresponding ϵ^* ranged from $\sim 10^{-9}$ to 10^{-5} m^2 s^{-3} in the upper few meters. Dissipation estimates corresponding to especially weak winds (less than 5 m s^{-1}) are substantially nosier than those corresponding to
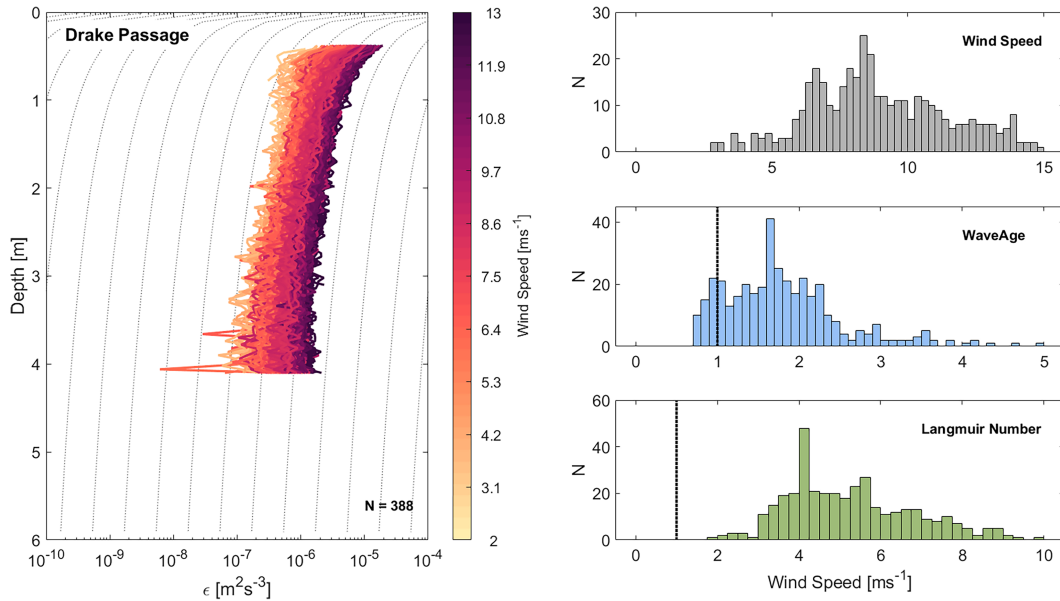
FIG. 9. As in Fig. 8, but for the Wave Glider data collected in the Southern Ocean.

strong winds, but still exhibit sorting based on wind speed. Wind speeds in the Southern Ocean ranged from 5 to 15 m s^{-1}; thus, there are no low-wind estimates of dissipation rate in the Wave Glider dataset. In general, ϵ^* estimates from the Southern Ocean are weaker than those obtained in the Southern California Bight at the same wind speeds. Histograms of wave age suggest that these differences may be due to the comparatively young seas in the Southern California Bight. Turbulent Langmuir numbers, (La$_*$) during both sets of observations were greater than 1. Here La$_*$ is defined as the square root of the ratio of friction velocity to Stokes drift. Friction velocity has been estimated from the observed wind speed assuming a classic drag law, and Stokes drift estimated from the observed peak wave period and frequency. However, La$_*$ were lower on average in the Southern California Bight and so conditions may have been more favorable to Langmuir overturning there as well.

Dissipation profiles derived from the high-pass filtered velocity (ϵ^+) are very similar to ϵ^*, except in the upper 1 m (Fig. 10b). We use data from the Southern California Bight to compare the different methods of estimating ϵ due to the greater range of
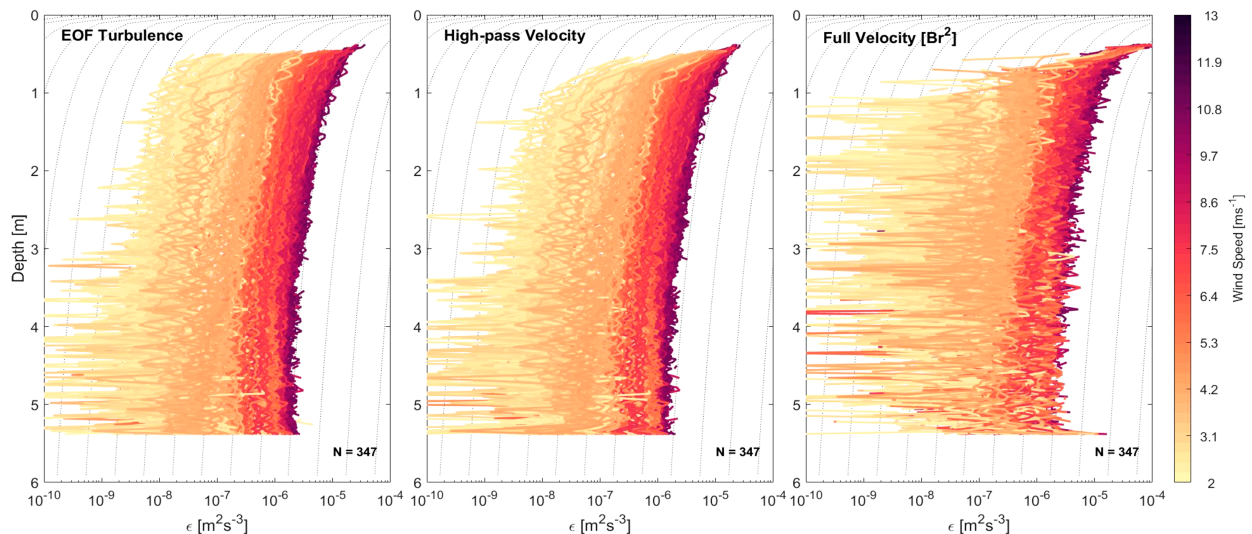

FIG. 10. Comparison between the different methods of estimating ϵ over the entire SWIFT dataset obtained in the Southern California Bight using the (left) EOF-filtered velocity, (center) high-pass filtered velocity, and (right) unfiltered velocity. The two prefiltered estimates are largely the same, with clear wind sorting. The unfiltered estimate is substantially nosier, which obscures much of the wind sorting at depth and at low wind speeds.

wind speeds observed there. Profiles of ϵ^+ are steeper than ϵ^* near the surface, deviating from z^{-1} at increasing depth with decreasing wind speed. In contrast to ϵ^* and ϵ^+, dissipation derived from the unfiltered velocity using the modified SF method (ϵ') are considerably nosier and not as neatly sorted by wind speed (Fig. 10b). There is almost no discernible wind speed dependence at the base of the profile. The mean MSPE of the analytically modified LSF to the unfiltered velocity is 12%, compared to 5% for both the EOF-filtered velocity and 1-m high-pass filtered velocity derived estimates.

6. Discussion

In this section we discuss our results before making final recommendations for analysis. We compare dissipation estimates which result from prefiltering the velocity data to remove wave shear with those from the analytically modified SF method. Our analysis suggests the former method produces estimates of $\epsilon(z)$ with reduced noise and a clear relationship to local wind speeds even under weak forcing conditions. We then test the sensitivity of ϵ^* to varying the number of EOFs used to construct an empirical wave profile and discuss limitations of the EOF filtering technique. Finally, we test the sensitivity of all versions of dissipation rate to varying the maximum separation scale used in the LSF (i.e., fitting range). We follow these discussions with a summary of our methodology and recommendations for analysis.

a. Advantages of prefiltering to remove wave bias

An important result of our analysis is the reduced noise and clear wind sorting of dissipation profiles derived from velocity data which have been prefiltered to remove wave bias, compared to those derived from the modified SF method of Scannell et al. (2017) (Fig. 10). This is likely due to the smaller fitting range enabled by filtering wave orbital velocities from the data. First, in the near-surface region we expect ϵ to increase by many orders of magnitude within a few meters, which limits the range of separation scales over which the LSF can be performed at any given depth. Distinguishing between r^2 and $r^{2/3}$ is substantially more difficult at fine scales. The mean square percent error of fitting r^2 against $r^{2/3}$ is less than 50% for $r_{max} \gtrsim 0.1$, but increases exponentially with decreasing fitting range (not shown). Second, the analytically modified LSF is inherently more sensitive to noise due to the additional degree of freedom introduced by the r^2 term.

More generally, the fundamental advantage of prefiltering techniques is that they are empirical and thus largely agnostic to the structure of the background flow. For example, the only assumption in performing the spatial high pass is that there is a separation in wavenumber space between nonturbulent shear and inertial subrange turbulence, which is consistent with the underlying Kolmogorov theory. This assumption is likely to fail very close to the surface, as in our example, where nonturbulent shear is strongest and edge effects of the filter are felt (Fig. 2e). In a related fashion, the EOF filter technique rests on the assumption that the dominant modes of variability are nonturbulent. In the case of surface waves, which have large vertical wavenumbers compared to the scales of turbulence, this has a similar effect as performing a spatial high

pass. However, the separation in wavenumber space is not a requirement for the EOF filter to be effective. We discuss advantages and limitations of the EOF analysis further in the next section.

The analytic formulation of the modified SF model is a strength specifically in the case of nonturbulent shear which is a straightforward superposition of linear surface gravity waves. The approximation given by Scannell et al. (2017) that leads to a structure function of the form r^2 is valid within 2% for the range of waves observed in these two datasets. However, if the background shear does not conform to the r^2 approximation the modified model will fail to account for bias in the structure function. This is more likely to occur in the very near surface, due to complex surface phenomena such as wave–current interactions, convective overturns, Langmuir turbulence, and diurnal stratified shear layers. In summary, the analytically modified SF model method is likely to perform well at depth in an environment dominated by approximately linear background shear, and which enables large fitting ranges. Near the surface, strong gradients in dissipation rate impose a limitation on the fitting range, which necessitates an empirical filtering technique that can remove nonturbulent shear *prior* to computing the structure function.

b. Sensitivity and limitations of EOF analysis

Surface gravity waves observed by downlooking ADCPs are well suited for EOF analysis because they are in phase across the "array" of ADCP depth bins as they propagate past the instrument. Further, the high resolution of the data means there are a large number of modes available to describe the system. The motion of the platform causes the deepest ADCP bins to be displaced up to 1 m horizontally between successive pings, but surface gravity waves with peak frequencies $O(0.1)$ Hz have wavelengths $O(100)$ m and subsequent space–time aliasing is small. Removing a few dominant modes from the data is akin to removing a strong background "mean" from each profile, with some near-surface curvature that is difficult to model analytically (Fig. 5). This is why EOFs are so similar to the spatial high pass. The "residual" is obviously not noise despite the bulk of the variance being contained in the first few EOFs (Fig. 4).

The main weakness in the EOF filtering technique is the subjective choice of what number of low-mode EOFs to remove from the data. In our example burst, frequency spectra of the EOF amplitudes reveal that only the first three EOFs have peaks in the wave band, thus providing a natural cutoff (Fig. 4). Such a detailed examination of the EOFs of each ADCP burst is not practical for bulk processing. However, varying the number of low-mode EOFs removed in the filter in the example burst case suggests that dissipation is likely robust to the choice between $\sim$2 and 6 EOFs (Fig. 11). The shape and magnitude of the profile is generally preserved up to the removal of 10 low-mode EOFs, except for a large decrease in ϵ around 0.5 m when more than 6 EOFs are removed (Fig. 11a). In fact, the estimate of $\epsilon(z)$ appears to improve when a few additional EOFs are removed, particularly near the surface where $\epsilon(z)$ was initially biased (Fig. 7). The best-fit power to the filtered velocity structure function
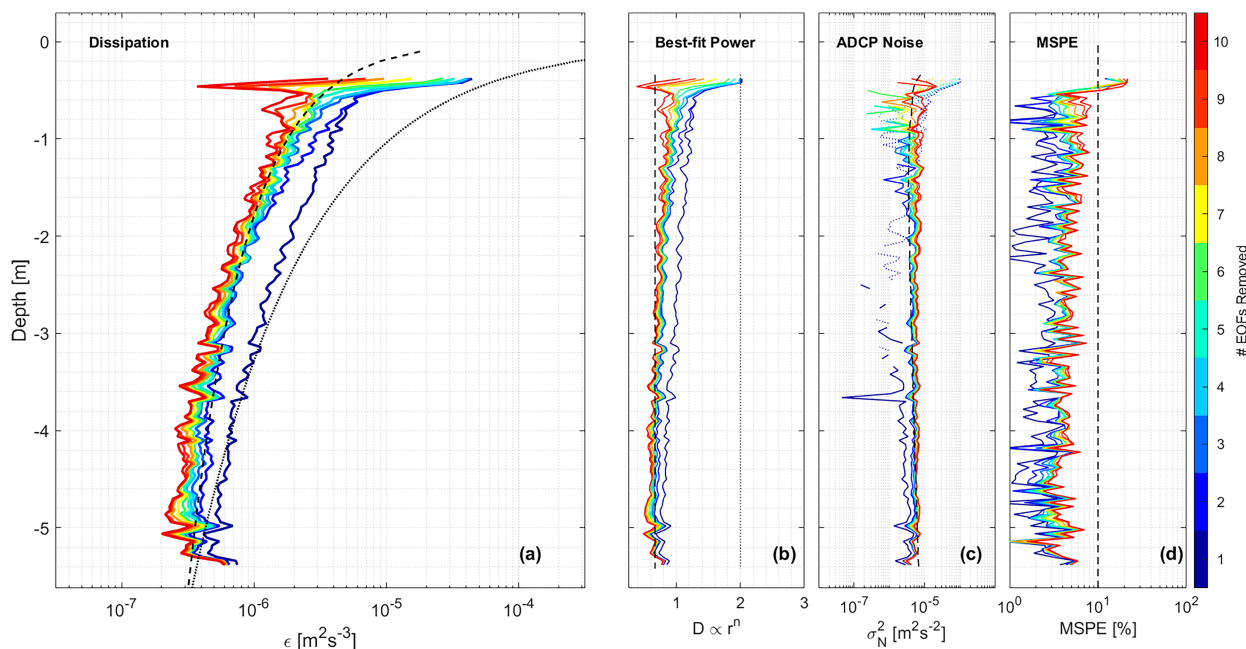
FIG. 11. Impact of varying the number of low-mode EOFs used to construct the wave profile, which is then removed from the data in the EOF filtering method. Subplots are as in Fig. 12, but here colored by number of EOFs removed from the data. The estimate of ϵ is robust to increasing the number of EOFs removed up to ∼6 for this example burst.

converges to $r^{2/3}$ and the estimate of ADCP noise becomes positive. However, MSPE increases slightly as additional low-mode EOFs are removed, likely due to the spatial-filter effect which is a consequence of the EOF sorting in wavenumber space (i.e., the redness of the wavenumber spectra). The removal of each additional low-mode EOF moves the local maximum in D^* to a smaller scale. The robustness of the dissipation estimate is not surprising, given the small separation scales used in the LSF. A fundamental assumption of the SF method of estimating dissipation is that the contribution to the structure function at each scale is primarily due to turbulent eddies at that scale, so even unintentional filtering of the largest scale turbulent velocities should not egregiously alter the results.

Finally, there are conditions under which we might expect the EOF filtering technique to fail. A weakness of the traditional EOF analysis is that signals must be in phase across the array due to the reliance on covariance at zero time lag, and so individual EOFs cannot represent the variability of vertically propagating modes (Merrifield and Guza 1990). Strong signals which propagate rapidly over the course of a burst may not be well described by low-mode EOFs, or may require the removal of a much greater number of low-mode EOFs. A few examples include internal waves, bubble plumes, and rapidly deepening shear layers. Potential improvements to the EOF filtering technique may include exploring alternatives which attempt to mitigate these phase-locked limitations, such as complex EOFs (Merrifield and Guza 1990).

c. Sensitivity to fitting range

To reduce uncertainty in our dissipation rate estimates we may include more data in the LSF by increasing the maximum separation scale (r_{max}) over which the fit is applied in each depth bin. However, reduced uncertainty comes at the expense of vertical resolution. Other potential issues include exceeding the upper limit of the inertial subrange and spreading the influence of any low-quality ADCP bins. Figure 12 illustrates how the three different estimates of dissipation rate are impacted by increasing r_{max} up to 0.64 m (16 vertical bins). ϵ^* decreases by a factor of 2 (except in the upper and lower 1 m of the profile) and develops $O(1)$ m vertical structure. This is consistent with the corresponding best-fit power to D^*, which remains very close to $r^{2/3}$. In contrast, ϵ^+ decreases by an order of magnitude uniformly with depth. Corresponding estimates of ADCP noise and MSPE increase with r_{max} as the shape of the structure function becomes progressively shallower than $r^{2/3}$. These differences between ϵ^* and ϵ^+ reflect the different local maxima in D^* and D^+ (Fig. 6). The latter occur at a precise separation scale of 0.5 m and so ϵ^+ decreases uniformly with increasing r_{max}. The vertical structure which appears in ϵ^* is due to the variability in the local maxima of D^*. Interestingly, ϵ' decreases uniformly with increasing r_{max} but appears to converge to the value given by the initial estimates of ϵ^+ and ϵ^* (i.e., using $r_{max} = 0.16$ m). This is consistent with the best-fit power to D', which converges to $r^{2/3}$. In all cases, the depth ranges influenced by the biased near-surface bins increases with r_{max}. These results of varying r_{max} confirm that it is prudent to keep the fitting range as small as possible.

7. Summary and recommendations for analysis

The primary contribution of this study is an update to the methodology of Thomson (2012) to compute profiles of turbulent dissipation rate from pulse-coherent high-resolution (HR)
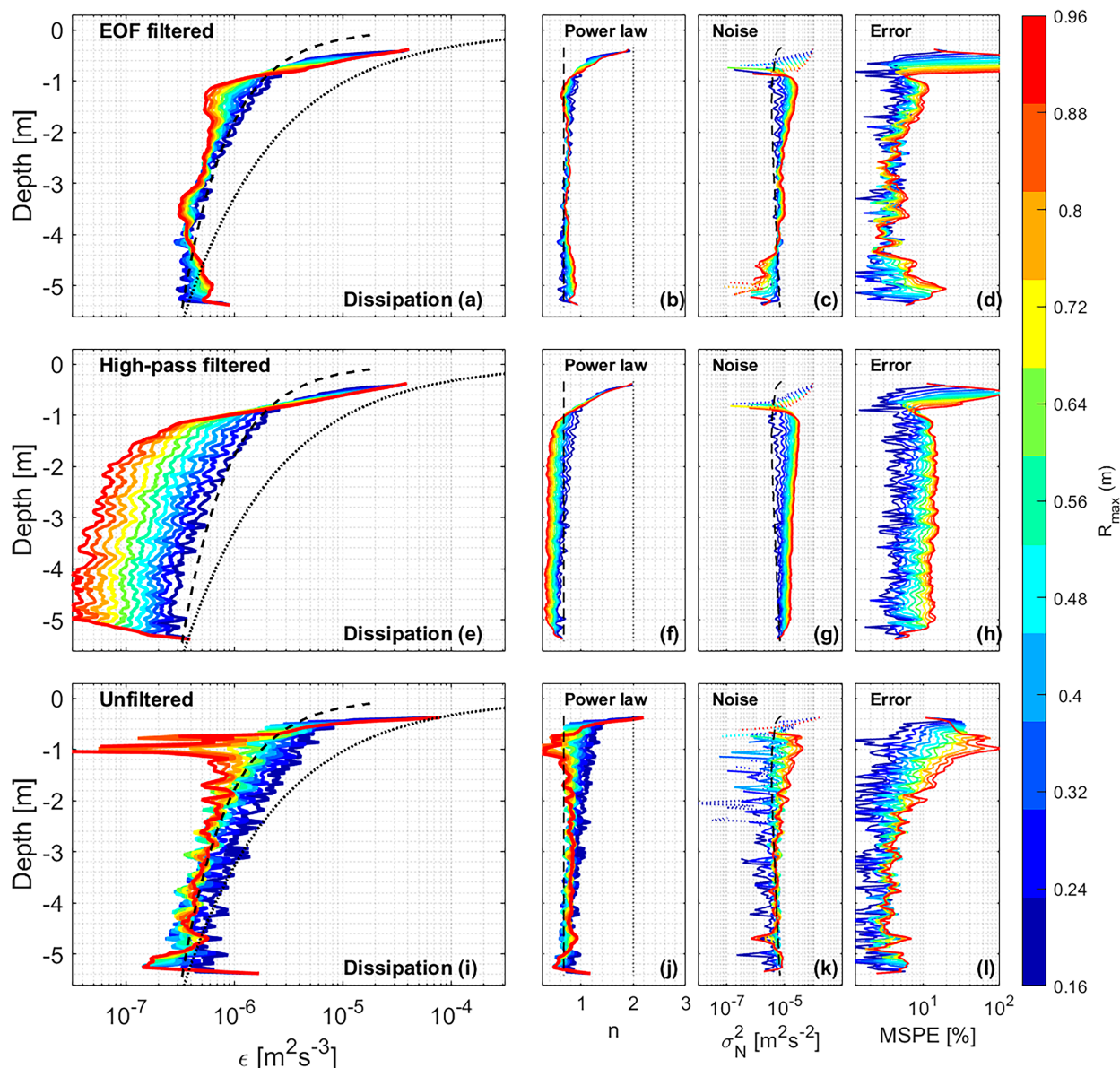
FIG. 12. Impact of varying the LSF fitting range, i.e., the maximum separation scale r_{max}, on (a),(e),(i) dissipation rate, (b),(f),(j) best-fit power to the structure function, (c),(g),(k) the estimate of ADCP noise produced by the fit, and (d),(h),(l) the MSPE of the fit. Results are derived from the (a)–(d) EOF-filtered velocity, (e)–(h) high-pass filtered velocity, and (j)–(l) unfiltered velocity. As in Fig. 7a, the dashed and dotted lines correspond to z^{-1} and z^{-2}, respectively. Line colors correspond to r_{max}, and in all cases, the MSPE increases with r_{max}.

ADCP data collected using surface-following platforms, building on the work of Scannell et al. (2017) to account for the bias in $\epsilon(z)$ generated by wave shear in the very near surface. As an alternative to the modified SF method put forward by those authors, we isolate the turbulent velocity signal from the wave orbital velocity using empirical methods. We compare two filtering techniques: a simple spatial filter that removes energy concentrated at low wavenumbers, and a modal filter that removes a time dependent wave profile computed using empirical orthogonal functions (EOFs) of the data. Our results suggest that the empirical filtering method produces dissipation estimates with

reduced noise compared to the modified SF method, which in turn reveals a clear relationship to local wind forcing otherwise obscured by noise at low wind speeds. We attribute the improved performance of the EOF filtering technique to the small separation scales necessitated by proximity to the sea surface, which constrains the number of points in the LSF. The analytic modification introduces an additional term to the structure function model and is therefore more sensitive to outliers due to the additional degree of freedom, while large fitting ranges are required to distinguish between the wave and turbulent terms. Based on the results of this study, we

recommend the following steps to compute dissipation rate from bursts of HR velocity data obtained using pulse-coherent mode on the central beam of a surface-following platform-mounted ADCP:

1) Despike the data (see appendix A).
   - Using an along-beam median high-pass filter, impose a threshold maximum velocity anomaly equal to half the phase-wrapping velocity (dependent on the instrument configuration; see Shcherbina et al. 2018, section 2c).
   - The best practice is to replace data spikes with NaN, since the structure function will be robust to missing data. However, interpolation may be necessary to retain enough points for an estimate of the EOFs (see step 2).

2) Filter out nonturbulent shear:
   (i) Option 1: Remove at least the two most energetic EOFs of the data.
       - The best practice is to examine the EOFs to determine an appropriate cutoff, though this may be impractical for bulk processing.
       - Interpolation through data spikes may be helpful in estimating the low-mode EOFs, but these points should be removed prior to computing the structure function.
   (ii) Option 2: Perform a spatial high pass to remove low-mode shear.
       This method will likely retain more surface wave shear with small decay scales in the very near surface than the EOF filter technique.

3) Compute the second-order velocity structure function (SF) of the data.
   - Produce squared velocity difference matrices for each along-beam velocity profile and average in time to produce a single burst-averaged second-order velocity SF matrix with bin-pair mean depth and separation scale dependence.
   - The best practice is to remove points which contain interpolated data prior to averaging. Interpolation is likely to alter the scale dependence of the subsequent SF (i.e., by removing energy at bin-scale separation).

4) Least squares fit the theoretical Kolmogorov model of the SF to the observed SF at discrete depths to obtain $\epsilon(z)$.
   - Bin the SF matrices by depth and perform a least squares fit against $r^{2/3}$ within each bin over a limited range of separation scales to obtain $\epsilon(z)$ from Eq. (2).
   - The best practice is to limit the maximum separation scale included in the fit as much as possible when along-beam variation in ϵ is expected to be large.
   - Some iteration may be required to determine the ideal fitting range, depending on the desired balance between resolution and reduced noise in the vertical.

5) Quality control $\epsilon(z)$.
   - The best practice is to use the mean-square percent error (MSPE) of the LSF.
   - The best-fit power law to the observed SF ($D \propto r^n$) may also be useful to evaluate how closely the measured turbulence adheres to the Kolmogorov prediction ($n = 2/3$), as well as the noise term in Eq. (2).

Throughout the manuscript we have commented on various user choices which may impact the results. The most significant is fitting range, but others include depth-bin size and number of EOFs included in the filter (alternatively the scale of the spatial high-pass filter). An additional sensitivity not explored in this manuscript are various definitions of the ensemble average, including the median and mean-of-the-log of the squared velocity differences. An argument may be made that the latter approach is more appropriate in light of the logarithmic distribution of dissipation scales, particularly in the near-surface environment (Gargett 1999). We have presented quality metrics to help evaluate the validity of $\epsilon(z)$, but a lingering uncertainty is what thresholds may be appropriate to apply. For example, in our data a threshold MSPE of 10% appeared organically but there is no inherent physical reason this value may distinguish between good and poor quality estimates. Although the relationship with local wind forcing provides confidence in our estimates, further improvements in this methodology would be significantly enhanced by comparison with direct in situ measurements of $\epsilon(z)$, wave-breaking crest distributions $\Lambda(c)$, or other hydrographic information such as stratification and horizontal velocity shear which can further help constrain the values we should expect from our analysis.

Data availability statement. The SWIFT data used in this study can be downloaded here: https://datadryad.org/stash/dataset/doi:10.5061/dryad.cvdncjt7s. The Wave Glider data can be found at http://hdl.handle.net/1773/49469. The codes used in data processing are publicly available at https://github.com/SASlabgroup/SWIFT-codes.

APPENDIX A

Raw Data Quality Control

Strong velocity spikes generate an inextricable bias in the burst-average structure function due to the squaring of velocity differences. Thus, despiking the velocity prior to analysis is necessary to reduce bias in the dissipation estimate. In pulse-coherent mode, along-beam velocity measured by the ADCP is a function of the phase shift between the pulse-pair echo with respect to their initial lag time. A well-known limitation of this method is ambiguity in the velocity introduced by phase shifts exceeding 2π, i.e., velocities which exceed a corresponding V_R. For the ADCP configuration used
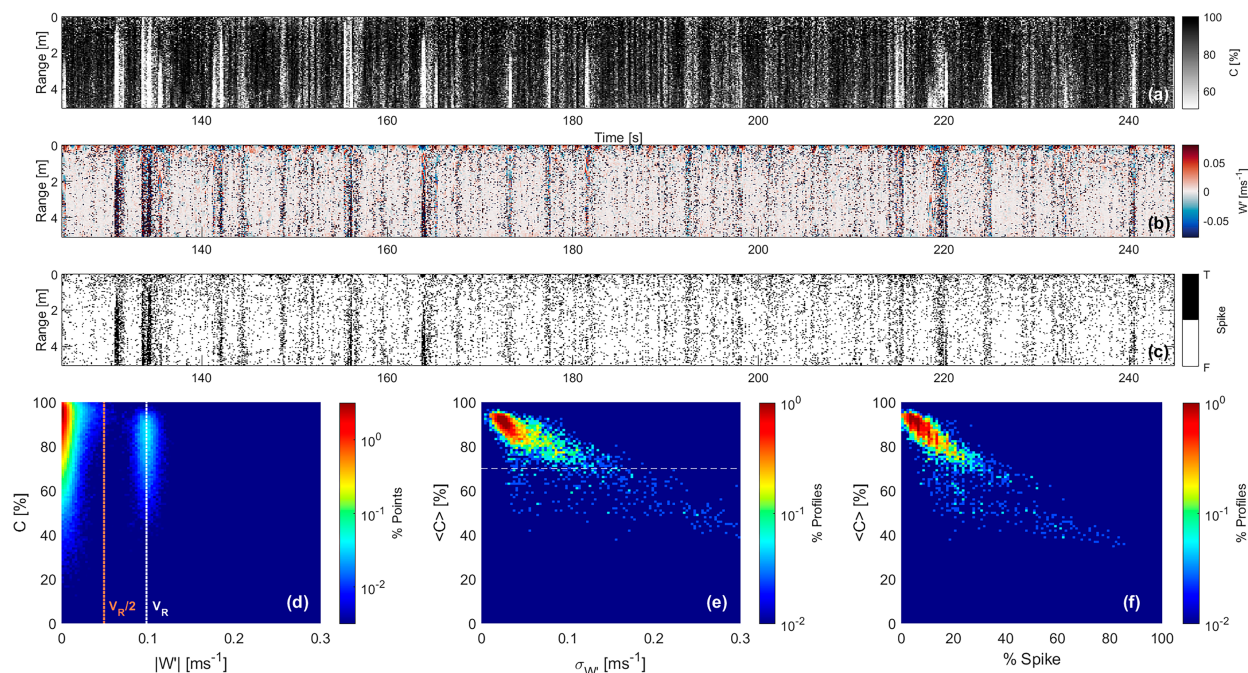
FIG. A1. Example of the despiking routine applied to the pulse-coherent Nortek Signature 1000 ADCP data. Shown are (a) pulse-pair correlation, (b) residual velocity after a 1 m median filter has been removed, and (c) data spikes, identified as residual velocities greater than $\pm V_R/2$. Also shown are probability density functions of the data as a function of (d) residual velocity magnitude vs pulse-pair correlation of each data point, (e) along-beam residual velocity variance vs profile-mean pulse-pair correlation, and (f) percent spikes per profile vs profile-mean pulse-pair correlation.

in this study, V_R is ~0.1 ms^{-1}. High velocities are susceptible to "phase wrapping," which manifests as velocity spikes equal to plus and minus an integer number of V_R. Ambiguity in the phase shift can also arise when the magnitude of the peak in lagged pulse-pair correlation (used to identify the phase shift) is weak. Figure A1 shows the data spikes identified in the example burst explored in sections 3 and 4, and their relationship to pulse-pair correlation. Correlation is generally about 80%, but low value points are littered throughout and the correlation over an entire ping will occasionally drop abruptly below 50% (Fig. A1a). These dropouts can last for ~1–10 pings (up to 1 s), during which the velocity is overwhelmed by strong spiking throughout the profile. It is common practice with ADCP data to use a minimum allowed correlation to identify bad data. However, because data spikes in the pulse-coherent ADCP data are driven by the strength of the velocity as well as the magnitude of the pulse-pair correlation, the pulse-pair correlation of each individual data point is not a sufficient predictor of individual data quality. Instead, spikes are identified by first removing a 1-m along-beam median filtered velocity from each profile (MATLAB's medfilt1, Fig. A1b). Spikes are flagged as residual velocities which exceed $\pm V_R/2$ (Fig. A1c). Figure A1d shows data probability density as a function of correlation and the 1-m median filtered velocity. There is a local maximum in the PDF at V_R and only a weak relationship with correlation. Although the relationship between velocity and correlation is weak for individual bins, profile-mean correlation is strongly correlated with the along-

beam variance in median-filtered velocity, and thus percent spikes per profile ($R = 0.85$, Figs. A1e,f). We flag bad pings using a minimum profile-average correlation value of 50%, and exclude them from further calculations. We do not employ the 2D phase-unwrapping technique of Shcherbina et al. (2018) here, as that method exploits temporal coherence of adjacent profiles of velocity. This approach is feasible in that study due to the neutral buoyancy of the profiling float, while in our study the strong platform motion of the SWIFT disrupts much of the temporal coherence. The resulting quality controlled data are shown in Fig. 2d. In the example burst, 10% of all profiles were flagged as bad.

APPENDIX B

Spectral Methods

Here we discuss reasons frequency and wavenumber spectra from a surface-following platform are likely to produce estimates of $\epsilon(z)$ with high error, using the example burst to illustrate. First, we address the use of frequency spectra. Two main challenges are 1) properly defining an advective velocity for a Lagrangian platform and 2) incoherence of the observed turbulent velocity fluctuations in time. The former makes the frozen-field assumption weak, and the latter smears the energy in frequency space. Previous authors have dealt with the problem of defining an advective velocity by obtaining an estimate of large-scale eddy self-advection from the velocity data (e.g.,
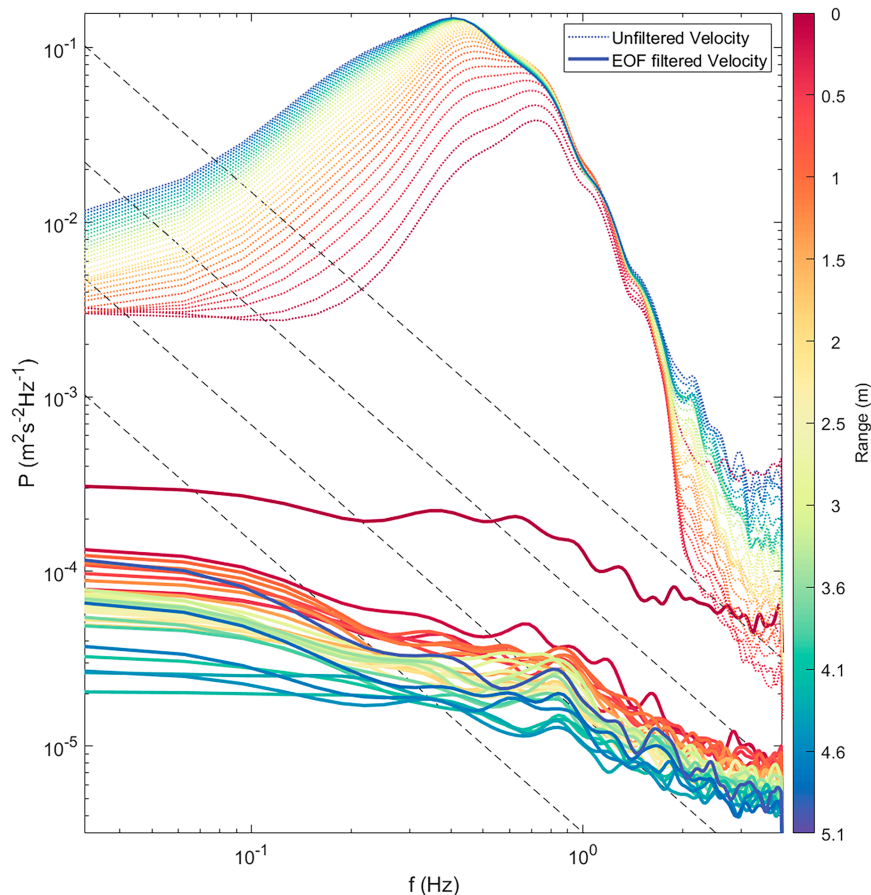
FIG. B1. Velocity–frequency spectra computed from the example burst as a function of depth bin, before and after wave orbital velocities are removed using the EOF filter technique (faded and bold lines, respectively). Initially, the spectra are contaminated by wave velocities across the entire resolved frequency range. After the wave velocities are removed, the residual spectra are much flatter than the expected $f^{-5/3}$ slope (dashed lines) expected for inertial subrange turbulence.

Zippel et al. 2018). However, this method does not account for advection by wave orbital motions and even if wave orbital velocities are successfully removed from the data, the coherence problem is likely intractable. Figure B1 shows frequency spectra computed from each ADCP bin in the example burst before and after wave orbital velocities are removed using the EOF filtering technique. Waves contribute spurious energy at all frequencies, which leads to an increase in energy with increasing distance from the transducer even at the high-frequency end of the spectra (i.e., away from the surface, pale lines). An increase in dissipation rate away from the surface is almost certainly not physical. As expected, removing wave orbital velocities from the data reverses the direction of increasing energy (now toward the surface, bold lines) and removes the broadband wave peak centered at 0.4 Hz. However, high-frequency tails of the residual spectra are much shallower than $f^{-5/3}$, consistent with smearing in frequency space due to the motion of the instrument. Tilt angles vary on average by a few to tens of degrees each ping, corresponding to horizontal

displacement of the ADCP beam by tens of centimeters up to 1 m. Near-surface length scales of turbulence are naturally limited by proximity to the sea surface to a few meters; thus, horizontal displacement $O(0.1)$ m between pings likely smears a large portion of the inertial subrange.

Wavenumber spectra may also be used to compute dissipation rate; however, only a single value of dissipation rate is obtained for an entire profile. Wavenumber spectra are also highly sensitive to strong data spikes, such as those characteristic of pulse-coherent ADCP data. This method is thus best suited for environments where background velocities are weak and the dissipation rate is expected to be constant over the profile range. For example, Shcherbina et al. (2018) computed wavenumber spectra with a clear $k^{-5/3}$ dependence using a Signature 1000 mounted on a subsurface Lagrangian float. As noted in appendix A, in that study the authors employ a "2D phase unwrapping" despiking technique that cannot be applied here due to platform motion. As a result, wavenumber spectra computed from individual velocity profiles in the example burst
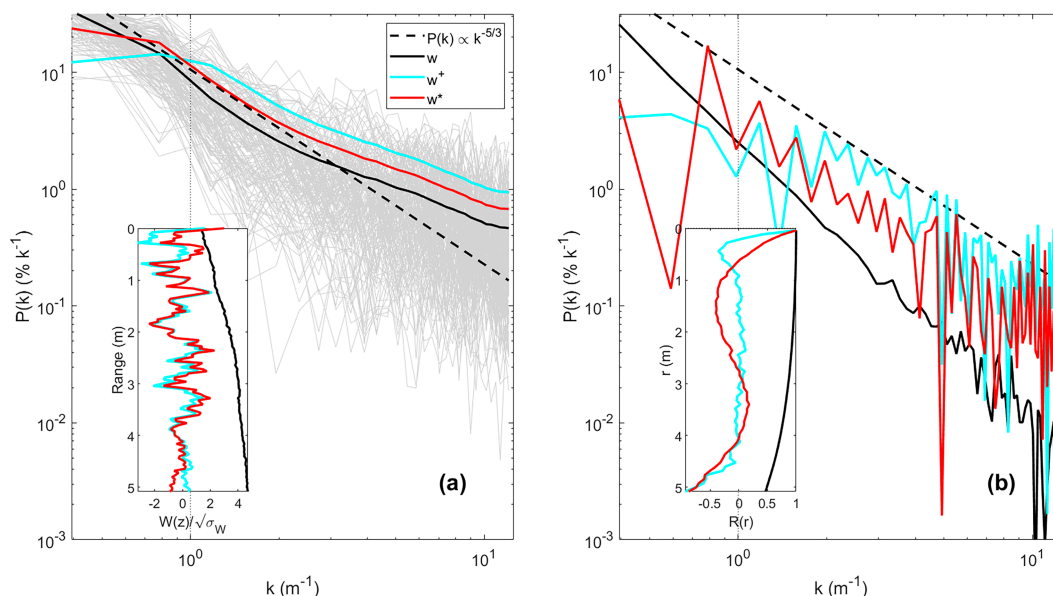
FIG. B2. Burst averaged along-beam velocity wavenumber power density spectra, computed (a) directly via Fourier transform of the along-beam velocity (thin gray lines) and then burst-averaged (bold lines), and computed (b) from the Fourier transform of the burst-averaged data–data pair autocorrelation function (bold lines). Inset in (a) shows examples of the velocity profiles on which the Fourier transform is performed. Inset in (b) shows the burst-averaged autocorrelation function on which the Fourier transform is performed, normalized by their variance. Black, red, and cyan lines correspond to the unfiltered (but quality-controlled) velocity, EOF-filtered velocity, and high-pass filtered velocity, respectively.

fluctuate wildly between an apparent noise floor and a lower limit that follows $\sim k^{-5/3}$ at high wavenumbers (Fig. B2a, thin gray lines). The resultant burst-averaged wavenumber spectra are shallower than $k^{-5/3}$ (bold lines).

An alternative method of computing wavenumber spectra is to take the Fourier transform of the along-beam autocorrelation. This method allows for averaging in time prior to performing the transform and is therefore more analogous to the structure function method, although it still produces a constant ϵ instead of a profile. The large N reduces the impact of any retained spikes and the resultant wavenumber spectrum has a clear $k^{-5/3}$ dependence at high wavenumbers (Fig. B2b). The autocorrelation-derived wavenumber spectra emphasizes a major strength of the structure function calculation: robustness in the face of poor data quality. Spectral methods require continuous time series and spikes must be filled in some fashion; thus, data with a high percentage of spikes are unusable. Because velocity differences are first averaged in time, structure functions can be computed even with a low percentage of "good" data. The quality metrics described in section 4 are then available to assess the accuracy of subsequent dissipation estimates.

REFERENCES

Belcher, S., and Coauthors, 2012: A global perspective on Langmuir turbulence in the ocean surface boundary layer. *Geophys. Res. Lett.*, **39**, L18605, https://doi.org/10.1029/2012GL052932.

Esters, L., O. Breivik, S. Landwehr, A. ten Doeschate, G. Sutherland, K. Christensen, J.-R. Bidlot, and B. Ward, 2018: Turbulence scaling comparisons in the ocean surface boundary layer. *J. Geophys. Res. Oceans*, **123**, 2172–2191, https://doi.org/10.1002/2017JC013525.

Gargett, A. E., 1999: Velcro measurement of turbulence kinetic energy dissipation rate. *J. Atmos. Oceanic Technol.*, **16**, 1973–1993, https://doi.org/10.1175/1520-0426(1999)016<1973:VMOTKE>2.0.CO;2.

Gemmrich, J., 2010: Strong turbulence in the wave crest region. *J. Phys. Oceanogr.*, **40**, 583–595, https://doi.org/10.1175/2009JPO4179.1.

Gerbi, G., J. Trowbridge, E. Terray, A. J. Plueddemann, and T. Kukulka, 2009: Observations of turbulence in the ocean surface boundary layer: Energetics and transport. *J. Phys. Oceanogr.*, **39**, 1077–1096, https://doi.org/10.1175/2008JPO4044.1.

Grare, L., N. Statom, N. Pizzo, and L. Lenain, 2021: Instrumented wave gliders for air-sea interaction and upper ocean research. *Front. Mar. Sci.*, **8**, 664728, https://doi.org/10.3389/fmars.2021.664728.

Guerra, M., and J. Thomson, 2017: Turbulence measurements from five-beam acoustic Doppler current profilers. *J. Atmos. Oceanic Technol.*, **34**, 1267–1284, https://doi.org/10.1175/JTECH-D-16-0148.1.

Hannachi, A., I. Jolliffe, and D. Stephenson, 2007: Empirical orthogonal functions and related techniques in atmospheric science: A review. *Int. J. Climatol.*, **27**, 1119–1152, https://doi.org/10.1002/joc.1499.

Hine, R., S. Willcox, G. Hine, and T. Richardson, 2009: The Wave Glider: A wave-powered autonomous marine vehicle. *Oceans*

2009, Biloxi, MS, IEEE, https://doi.org/10.23919/OCEANS.2009.5422129.

Hughes, K., J. Moum, E. Shroyer, and W. Smyth, 2021: Stratified shear instabilities in diurnal warm layers. *J. Phys. Oceanogr.*, **51**, 2583–2598, https://doi.org/10.1175/JPO-D-20-0300.1.

Kolmogorov, A. N., 1941: Dissipation of energy in the locally isotropic turbulence. *Dokl. Akad. Nauk SSSR*, **30**, 301–305.

Lucas, N. S., J. H. Simpson, T. P. Rippeth, and C. P. Old, 2014: Measuring turbulent dissipation using a tethered ADCP. *J. Atmos. Oceanic Technol.*, **31**, 1826–1837, https://doi.org/10.1175/JTECH-D-13-00198.1.

McMillan, J. M., A. E. Hay, R. G. Lueck, and F. Wolk, 2016: Rates of dissipation of turbulent kinetic energy in a high Reynolds number tidal channel. *J. Atmos. Oceanic Technol.*, **33**, 817–837, https://doi.org/10.1175/JTECH-D-15-0167.1.

Merrifield, M., and R. Guza, 1990: Detecting propagating signals with complex empirical orthogonal functions: A cautionary note. *J. Phys. Oceanogr.*, **20**, 1628–1633, https://doi.org/10.1175/1520-0485(1990)020<1628:DPSWCE>2.0.CO;2.

Mohrholz, V., H. Prandke, and H. Lass, 2008: Estimation of TKE dissipation rates in dense bottom plumes using a pulse-coherent acoustic Doppler profiler (PC-ADCP)—Structure function approach. *J. Mar. Syst.*, **70**, 217–239, https://doi.org/10.1016/j.jmarsys.2007.03.004.

Scannell, B. D., T. P. Rippeth, J. H. Simpson, J. A. Polton, and J. E. Hopkins, 2017: Correcting surface wave bias in structure function estimates of turbulent kinetic energy dissipation rate. *J. Atmos. Oceanic Technol.*, **34**, 2257–2273, https://doi.org/10.1175/JTECH-D-17-0059.1.

Shcherbina, A. Y., E. A. D'Asaro, and S. Nylund, 2018: Observing finescale oceanic velocity structure with an autonomous Nortek acoustic Doppler current profiler. *J. Atmos. Oceanic Technol.*, **35**, 411–427, https://doi.org/10.1175/JTECH-D-17-0108.1.

Sutherland, P., and W. K. Melville, 2015: Field measurements of surface and near-surface turbulence in the presence of breaking waves. *J. Phys. Oceanogr.*, **45**, 943–965, https://doi.org/10.1175/JPO-D-14-0133.1.

Taylor, G. I., 1937: The statistical theory of isotropic turbulence. *J. Aeronaut. Sci.*, **4**, 311–315, https://doi.org/10.2514/8.419.

Terray, E., M. Donelan, Y. Agrawal, W. Drennan, K. Kahma, A. Williams, P. Hwang, and S. Kitaigorodskii, 1996: Estimates of kinetic energy dissipation under breaking waves. *J. Phys. Oceanogr.*, **26**, 792–807, https://doi.org/10.1175/1520-0485(1996)026<0792:EOKEDU>2.0.CO;2.

Thomson, J., 2012: Wave breaking dissipation observed with SWIFT drifters. *J. Atmos. Oceanic Technol.*, **29**, 1866–1882, https://doi.org/10.1175/JTECH-D-12-00018.1.

——, M. S. Schwendeman, S. F. Zippel, S. Moghimi, J. Gemmrich, and W. E. Rogers, 2016: Wave-breaking turbulence in the ocean surface layer. *J. Phys. Oceanogr.*, **46**, 1857–1870, https://doi.org/10.1175/JPO-D-15-0130.1.

——, J. Girton, R. Jha, and A. Trapani, 2018: Measurements of directional wave spectra and wind stress from a Wave Glider autonomous surface vehicle. *J. Atmos. Oceanic Technol.*, **35**, 347–363, https://doi.org/10.1175/JTECH-D-17-0091.1.

Wiles, P., T. P. Rippeth, J. Simpson, and P. Hendricks, 2006: A novel technique for measuring the rate of turbulent dissipation in the marine environment. *Geophys. Res. Lett.*, **33**, L21608, https://doi.org/10.1029/2006GL027050.

Zippel, S. F., J. Thomson, and G. Farquharson, 2018: Turbulence from breaking surface waves at a river mouth. *J. Phys. Oceanogr.*, **48**, 435–453, https://doi.org/10.1175/JPO-D-17-0122.1.